Highlights of Collaborated Research

Collaborative works with outside researches are carried out in consideration of the joint research program. Accepted applications are performed in following each division and facility of IMR.

1) Research Laboratories

Joint research conducted by out side researchers and IMR staff members at each research laboratory. Three categories; “Research in priority areas”, "General Research" and “Exploratory Research for Young Researchers” are prepared.

2) International Research Center for Nuclear Materials Science

This facility is open to university scientists all over Japan to support experiments using Japan Materials Testing Reactor, JMTR, the fast experimental reactor, JOYO, and the test reactor, JRR-3, operated by JAEA (Japan Atomic Energy Agency). The overseas reactor, BR2, located at the Belgian Nuclear Research Center, is also used for irradiation experiments. This facility acts as a hub for international collaborations; specimens irradiated in overseas reactors are accepted here for post-irradiation examinations by participating university researchers. Research subjects covered here include fundamental studies and R&D on fusion structural materials, high heat-flux materials, and a variety of functional materials, as well as engineering-oriented studies for the safety of light water reactors and basic researches supporting them. Materials studies utilizing radio-isotopes are also being conducted.

3) Advanced Research Center of Metallic Glasses (ARCMG)

ARCMG originates from the Laboratory for Advanced Materials (LAM) established in 1986 for “the investigation and application of scientific principles of materials.” This laboratory was composed of two major divisions, scientific research on fundamental properties of materials and engineering approach for industry. Since it was recommended that we should further promote research on bulk metallic glasses, we decided to set up the ARCMG in April 2006. Micromotors, pressure sensors, fuel cell separators, soft magnetic materials and many other devices that use bulk metallic glasses are about to become practical propositions.

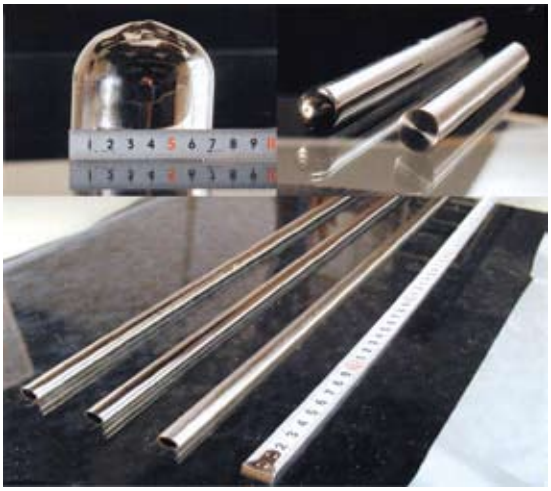

4) High Field Laboratory for Superconducting Materials

This laboratory restarted in 2001, succeeding “High Field Laboratory for Superconducting Materials” which was established in 1981. The main equipment is a hybrid magnet which generates steady high magnetic fields up to 31T. In addition, many cryogen-free superconducting magnets which have been developed by our laboratory are installed. Especially, we succeeded in developing the world’s first cryogen-free hybrid magnet, which generates 27.5 T. The laboratory also provides instruments for measuring various physical properties. These facilities are open to scientists and engineers on superconductors and other materials research.

5) Osaka Center for Industrial Materials research

The Osaka Center was established at Osaka as a special unit in IMR in April 2006 based on the agreement between Tohoku University and Osaka Prefecture Government. It is a laboratory dedicated to research and development of nano-structured metallic materials from the application viewpoints based on the basic research in the material science, chemistry and physics associated with research organizations in the Kansai region. Research in the Osaka Center is focused in particular on the understanding of the fundamental properties of nano-structured metallic materials and the rapid realization of their application to industry, in particular, the small and medium enterprises in Osaka area.

6) Center for Computational Materials Science

This center was developed from the Laboratory of Materials Information Science which was established in February 1989. Its main tasks are 1) administration and maintenance of the supercomputing system in this Institute, 2) maintenance of a supercomputing system network, 3) general support for the usage of the supercomputing system, 4) support of materials design by supercomputing simulation with vectorization and parallelization, 5) construction of factual database for materials in nonequilibrium phase , and 6) support of activity of Nanotechnology group on SINET3 and Asian Consortium for Materials Science, ACCMS-VO.

7) International Collaboration Center (ICC-IMR)

This Center was established in April 2008. The mission is to serve as an international center for materials research and to encourage the international collaboration on researches of IMR. The International School on advanced materials, international workshops are coordinated. The Center hosts the foreign visiting scientists who collaborate on research with members of IMR.

Effect of Electron-Phonon Interaction on Photoexcited States of One-Dimensional Mott Insulators

Interplay of strong electron correlation and electron-phonon (EP) interaction is one of important issues in the physics of low dimensional correlated electron systems. In order to understand the interplay, we theoretically examine the optical properties of the one-dimensional (1D) Mott insulators, and clarify the effect of the EP interaction on their photoexcited states.

The interplay of strong electron-electron correlation and EP interaction has recently attracted much attention. One of the issues is to understand the effect of the EP interaction on carriers introduced into a Mott insulator. In the ground state of the Mott insulator, the on-site Coulomb repulsion, U, makes the charge distribution uniform, and then the EP interaction is irrelevant. However, the mobile carriers created in the Mott insulator by chemical and/or photo dopings induce the charge fluctuation, and thus the EP interaction is expected to play an important role in various physical quantities.

The charge gap in Mott insulators is a consequence of strong electron correlation represented by large U. The correlation induces novel phenomena in terms of the interplay of charge and spin degrees of freedom. In 1D Mott insulators such as Sr_2CuO_3, two particles created by photo-excitation, i.e., an unoccupied site and a doubly occupied site of electrons can move inside the system without being disturbed by surrounding spins in the background. This is a manifestation of a separation of the charge and spin degrees of freedom, called the spin-charge separation inherent in 1D correlated electron systems. Optical responses in the 1D Mott insulators are characterized by this phenomenon. However, recently discovered ultra fast relaxation of photoexcited state in 1D Mott insulators cannot be understood by the spin-charge separation. Rather, ordinal EP interaction between charge and phonon should be important (Fig.1). Therefore, it is crucial to clarify interplay of electron correlation and EP interaction in 1D Mott insulators. This is also important for designing a new type of optical switches utilizing the 1D Mott insulators.

We apply a dynamical density matrix renormalization group to a Hubbard-Holstein model at half filling and calculate

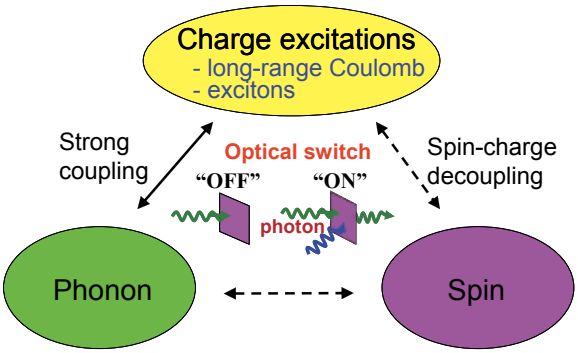

Fig. 1 A view of relation among charge, spin and, phonon degrees of freedom in the process of photoexcitation of 1D Mott insulators. This relation is crucial for optical switches utilizing 1D Mott insulators.

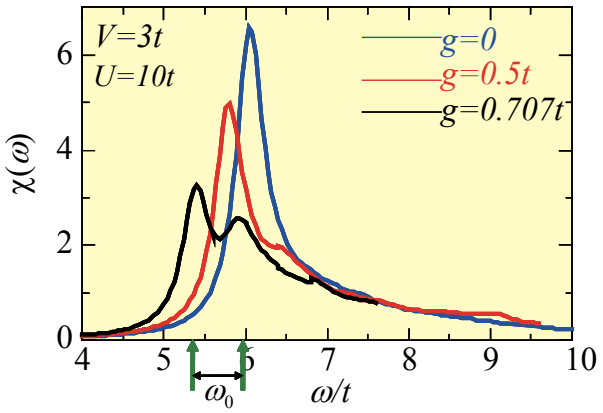

Fig. 2 Current-current correlation function in a 20-site chain of one-dimensional Hubbard-Holstein model at half filling. An excitonic peak at ω=6t for zero EP coupling (g=0), which is induced by a nearest-neighbor Coulomb interaction V, shifts to the low-energy side and splits into two peaks separated by a phonon frequency ω_0 with increasing g.

current-current correlation function χ(ω) that is proportional to absorption spectrum [1]. Figure 2 shows the dependence of χ(ω) on a EP coupling constant g for a 20-site Hubbard-Holstein chain with U=10t, a nearest-neighbor (NN) Coulomb interaction V=3t, and an Einstein phonon frequency ω_0=0.5t, t being NN hopping interaction. Without g, an excitonic peak appears at an excitation energy of ω =6t. With increasing g, the peak shifts toward the low-energy side. For a realistic value of g for Sr_2CuO_3 (g=0.707t), the excitonic peak splits into two peaks whose separation is close to ω_0. This is qualitatively consistent with a broaden feature of absorption spectrum of Sr_2CuO_3, although a two peak feature has not been observed.

We also examine U dependence of χ(ω) in detail [1] and find that the effect of the EP interaction on an exciton is enhanced by increasing U. This enhancement is in contrast to the effect of the EP interaction on the ground state, wherein the Peierls instability is suppressed by U, and thus indicates a crucial role of phonon degree of freedom in the photoexcited states of 1D Mott insulators.

References

[1] H. Matsueda, A. Ando, T. Tohyama and S. Maekawa, Phys. Rev. B **77**,193112 (2008).

Key Words

Mott Insulator, Optical Properties, Electron-Phonon Interaction

Contact to
Takami Tohyama (Yukawa Institute for Theoretical Physics, Kyoto University)
e-mail: tohyama@yukawa.kyoto-u.ac.jp
Sadamichi Maekawa (Theory of Solid State Physics Division)
e-mail: maekawa@imr.tohoku.ac.jp

In-plane Conduction and *c*-axis Polarization in the Misfit-layered Oxide $[Bi_2Ca_2O_4]_qCoO_2$

We have used low-frequency dielectric measurements to study the evolution of anisotropic charge transport in misfit layered oxides $[Bi_2Ca_2O_4]_qCoO_2$. Above ~60 K, the in-plane dc conductivity obeys the Arrhenius law and the dielectric polarization occurs along the c direction. We point out that this c-axis polarization is attributed to the activated carrier which is confined to ab plane.

The different temperature dependence between in-plane and out-of-plane charge transport is observed on a number of layered materials. Especially in the studies of high-T_c cuprates, the discrepancy is called the "charge confinement" in connection with the strong electron correlations or the pseudogap phenomena. In order to gain insight into the origin of the anisotropic behavior, it is worthwhile to investigate the evolution of anisotropic charge transport in various types of layered insulators. The low-frequency dielectric measurement is appropriate for this purpose because it provides relevant information about the electrical conduction, the dielectric polarization and the effects of disorder [1].

A misfit-layered cobaltite $[Bi_2Ca_2O_4]_qCoO_2$ is an insulating end member of Bi-*M*-Co-O (*M*=Ca, Sr, Ba) systems. We succeeded in growing $[Bi_{2+0.52}Ca_{2-0.52}O_4]_{0.627}CoO_2$ single crystals using the flux method. Figure 1(a) shows the temperature dependence of the in-plane resistivity ρ_{ab}. The insulating behavior is observed at all measured temperatures. In the high-T region, ρ_{ab} obeys the thermal activation formula with an activation energy of ~32 meV (Fig. 1(b)). In the low-T region, the data coincide with Mott variable-range hopping formula for a noninteracting Fermi glass (Fig. 1(c)), indicating the existence of the localized states due to some disorders. The crossover temperature T^* is estimated to be 63 K.

Out-of-plane dielectric spectra ε'_c are shown in Fig. 2. With increasing temperature, the rapid ε'_c growth is visible in the lower frequencies (below ~10^4 Hz), reaching 5×10^4 at 20 Hz and 250 K. As the high voltage is applied, the ε'_c swells are completely suppressed and turn to negative values [2]. This result implies that the observed polarizability growth is closely related to an increase in the mobile carrier number,

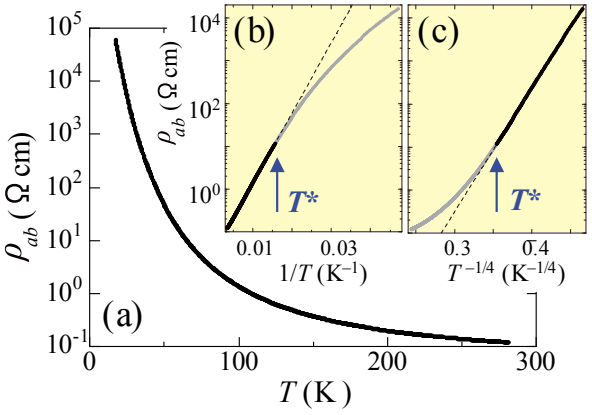

Fig. 1 (a) Temperature dependence of ρ_{ab}. The same data are plotted against $1/T$ in (b) and $T^{-1/4}$ in (c).

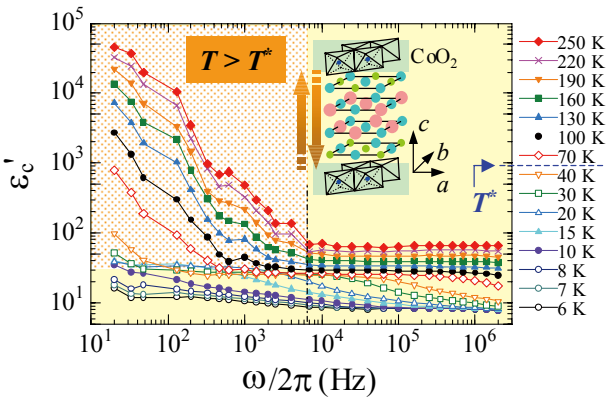

Fig. 2 Frequency dependence of the dielectric constant ε'_c. A conceptual figure of *c*-axis polarization is shown by arrows in the inset.

that is, under the strong field the short-range localized (dielectric) carriers move across potential barriers and have the screening ability. Note that ε'_c appears to rise from the vicinity of T^*, above which the thermally activated behavior becomes dominant within the *ab* plane. Our observation indicates that the *c*-axis polarization is attributed to the activated carriers, which stay within the *ab* plane even if they can excite across the in-plane energy gap. We expect that the observed out-of-plane dielectric phenomenon will provide a clue to the understanding of the mechanisms underlying the anisotropic charge localization.

References

[1] M. Maki, S. Nakao, K. Machida, M. Shiraishi, X.-G. Zheng, T. Naito and H. Iwasaki, J. Phys. Soc. Jpn. **76**, 044711 (2007)

[2] M. Maki, K. Machida, T. Mori, T. Nishizaki and N. Kobayashi, Phys. Rev. B **78**, 073101 (2008)

Key Words

Localization, Dielectric Property, Misfit-layered Cobaltite

Contact to
Makoto Maki (Department of Physics, Saga University)
e-mail: mmaki@cc.saga-u.ac.jp
Norio Kobayashi (Low-Temperature Physics Division)
e-mail: koban@imr.tohoku.ac.jp

Relationship Between Crystal Structure and Superconductivity in Iron-based Superconductors

Recently, iron-based superconductors have attracted great attention as new high-Tc materials. We have clarified that there is a strong relationship between crystal structure and superconductivity using neutron diffraction technique. Characteristically, superconducting transition temperatures attain maximum values when $FeAs_4$-tetrahedrons form a regular shape.

Recent discovery of superconductivity in $LaFeAsO_{1-x}F_x$ at superconducting temperature of T_c=26K has triggered the energetic study of searching a new superconductor. Soon, it has been found that fluorine-free $LnFeAsO_{1-y}$ (Ln=lanthanoid) samples show superconductivity with maximum T_c=55K. As the T_c is very high, their cooper pairing mechanism could not be explained by the conventional BCS theory. To elucidate the mechanism, their crystal structure should be determined.

The crystal structure of LnFeAsO is characterized by two kinds of stacking layers LnO and FeAs (Fig. 1). The Fe atom is surrounded by four As atoms in the FeAs layer forming a $FeAs_4$ tetrahedron. Charges are transferred from LnO to FeAs layers by substitution or introduction of defect of oxygen atoms. We focus our attention on crystal structure of FeAs layers, since superconductivity is induced in FeAs layers.

We conducted neutron diffraction measurements using high-resolution powder diffractometer D2B of the ILL in Grenoble, France and HERMES of the Institute for Materials Research, Tohoku University, installed at the JRR-3 reactor of JAEA at Tokai. The obtained spectra were analyzed by the Rietveld method. Polycrystalline samples of $LnFeAsO_{1-y}$ (Ln=La, Ce, Pr, Nd, Tb and Dy) were used for the measurements.

We have clarified the superconducting phase diagram of $LaFeAsO_{1-y}$ and $NdFeAsO_{1-y}$ by estimating the oxygen content. Both systems show superconductivity above y~0.06. But, doping dependence of T_c is different. In $LaFeAsO_{1-y}$, T_c attains maximum values at around y=0.12 and decreases with increasing y. Whereas in $NdFeAsO_{1-y}$, T_c increases till y=0.26. It seems that there is no universal relationship between T_c and carrier concentration.

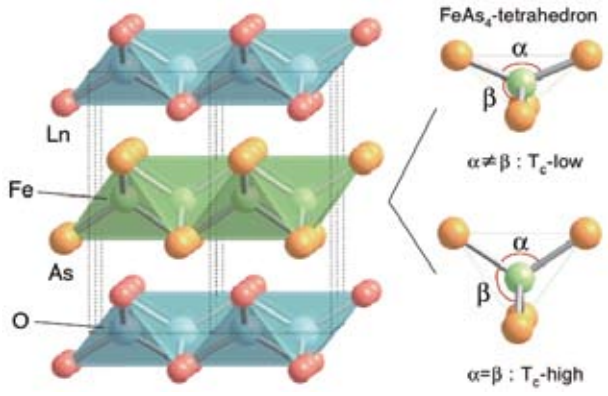

Fig. 1 The crystal structure of LnFeAsO. The dashed lines show unit cells. $FeAs_4$ clusters in the FeAs layers form a tetrahedral lattice. T_c reaches maximum when the $FeAs_4$-lattices form a regular tetrahedron [2].

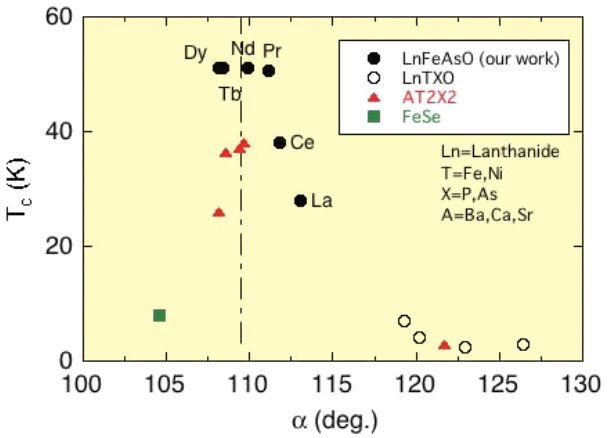

Fig. 2 T_c vs As-Fe-As bond angle α for various pnictide superconductors. Crystal structure parameters of samples showing almost maximum T_c in each system are selected. The vertical dashed line indicates the bond angle of a regular tetrahedron (α = 109.47°).

Figure 2 shows As-Fe-As bond angle as a function of T_c in various pnictide superconductors [1]. The parameters of the samples showing almost maximum T_c in each system are selected to eliminate the effect of carrier doping. The obtained lanthanoid dependence of crystal structure parameters in $LnFeAsO_{1-y}$ system shows that $FeAs_4$-tetrahedrons form a regular shape around $NdFeAsO_{1-y}$. Obviously, T_c becomes maximum when $FeAs_4$-tetrahedrons form a regular shape, indicating that there is a strong correlation between crystal structure and superconductivity.

References

[1] C. H. Lee, A. Iyo, H. Eisaki, H. Kito, M. T. Fernandez-Diaz, T. Ito, K. Kihou, H. Matsuhata, M. Braden, and K. Yamada, J. Phys. Soc. Jpn. **77**, 083704 (2008).

[2] C. H. Lee, A. Iyo, H. Eisaki, H. Kito, M. T. Fernandez-Diaz, R. Kumai, K. Miyazawa, K. Kihou, H. Matsuhata, M. Braden and K. Yamada, J. Phys. Soc. Jpn. **77**, 44 (2008) Suppl. C.

Key Words

Iron Pnictides Superconductivity, Powder Neutron Diffraction, Crystal Structure Analysis

Contact to
Chul-Ho Lee (Advanced Industrial Science and Technology (AIST))
e-mail: chlee@aist.go.jp
Kazuyoshi Yamada (Metal Physics with Quantum Beam Spectroscopy Division)
e-mail: kyamada@imr.tohoku.ac.jp

Effect of Austenite Grain Boundaries on the Morphology of Lath Martensite

Lath martensite is an important structure for strengthening and adding toughness to steels. The growth process and key factors of the morphology, which are important to development of martensitic steels, have not been understood. Our purpose is to clarify the key factor in the morphology of lath martensite.

Lath martensite in steel is well known to show a hierarchical microstructure consisting of packets, blocks, sub-blocks, and laths. The prior austenite grain is divided into packets that consist of blocks. These blocks within the packets have the same habit plane. The packet is further divided into plate like blocks, which consist of laths with a similar crystal orientation. Recently, it has been recognized that a block contains components called sub-blocks, each of which corresponds to a single variant characterized by the Kurdjumov-Sachs orientation relationship (KS OR) with austenite, as shown in Fig. 1 [1].

The complex microstructure affects the mechanical properties, and control of the growth process of the microstructure is necessary for microstructural control. The growth process of the microstructure has not been clarified, although controlling the microstructure is important. To understand the growth process, characterization of the initial structure of lath martensite, i.e., the rule of the nucleation is important because martensite laths and plates appear like autocatalysis nucleation following the initial martensite laths. From previous reports [2], the austenite grain boundaries and annealing twin boundaries are known to be effective nucleation sites for martensite. However, the nucleation rule for lath martensite is still unclear. The present work focused on the characterization of the initial structure of lath martensite, using local crystallographic analyses, and found the rule of the initial structure [3].

The specimens used were partially transformed lath martensite in an Fe-Ni-Mn alloy. The crystallography of the lath martensite was examined by scanning electron microscopy/electron backscatter diffraction pattern analysis (SEM/EBSD) and transmission electron microscopy/Kikuchi pattern analysis (TEM/KP).

Figure 2(a) shows an optical micrograph of lath martensite

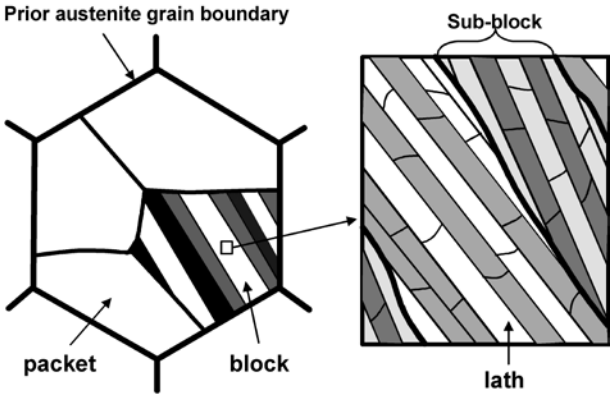

Fig. 1 Schematic illustration of lath martensite [1].

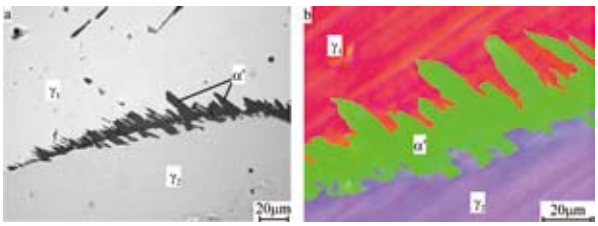

Fig. 2 (a) Optical micrograph with 3% nital etching and (b) orientation image map measured on the Fig. 2 (a) with SEM/EBSD in the Fe-Ni-Mn alloy. The crystal orientations of martensite plates in both austenite grains are similar.

in the Fe-Ni-Mn alloy. The etched and non-etched regions are lath martensite and austenite regions, respectively. There are two austenite grains, i.e., γ_1 and γ_2. The lath martensite regions (α') appear around the austenite grain boundary and grow into both austenite grains. The orientation image map measured with SEM/EBSD in Fig. 2(b), which is the same region shown in Fig. 2(a), indicates that the crystal orientations are similar in the martensite plates in both austenite grains. Other observations showed that lath martensite appears around the high angle austenite grain boundaries and annealing twin boundaries. From these observations and crystallographic analyses, the rules of initial lath martensite were found: 1) Martensite laths held KS OR with austenite and the other austenite grains; 2) the parallel closed packed direction of the KS OR held by the martensite lath is nearly parallel to the austenite grain boundaries; and, 3) the transformation shear and misfit strain can be accommodated effectively along the austenite grain boundaries or by slip in the other austenite grain.

References

[1] S. Morito, X. Huang, T. Furuhara, T. Maki and N. Hansen: Acta Mater. **54**, 5323 (2006).

[2] e.g., K. Tsuzaki and T. Maki: J. Jpn. Inst. Metals, **45**, 126 (1981).

[3] S. Morito, J. Nishikawa, T. Ohba, T. Furuhara and T. Maki: *Proc. of Int. Conf. on Martensitic Transformations 2008*, Santa Fe, NM, USA, 2008.7.1, in press.

Key Words

Lath Martensite, Local Crystallographic Analysis, 3D Analysis

Contact to
Shigekazu Morito (Department of Materials Science, Shimane University)
e-mail: mosh@riko.shimane-u.ac.jp
Tadashi Furuhara (Microstructure Design of Structural Metallic Materials Division)
e-mail: furuhara@imr.tohoku.ac.jp

Hydrogen Retention Properties on the Divertor Tiles in LHD

Surface modification and hydrogen retention of a LHD divertor tile used for plasma experiments for 8 years were analyzed by using the ion beam analytical techniques. On the deposition dominant area, surfaces were covered mainly with Fe and Ti, respectively. In this area, the amount of hydrogen retention was relatively high, while, on the erosion dominant area, hydrogen retention was much lower than that of the deposition area.

One of the key issues for the establishment of a steady state fusion reactor system is impurity control. A continuous, long-lasting plasma erodes a significant amount of the plasma facing components (PFCs) on the one hand, and a corresponding amount of deposits is formed on PFCs. In general, deposited layers are unstable and therefore they are a possible source of impurity (dust) for the plasma. The deposited layers and the dusts can retain a huge amount of tritium. Such mobile products as dust with a radiation isotope are the source of another critical concern in a fusion reactor. In Large Helical Device (LHD), the first wall panels and divertor plates are made of stainless steels and isotropic graphite, respectively, uncontrollable plasma density rise occurred in long pulse discharges with ion cyclotron heating due to hydrogen outgas locally induced by heating of the divertor tile in a discharge [1]. Therefore, quantitative data of retained hydrogen in the divertor tiles is important for the steady state plasma operation in LHD as well as for tritium inventory in the future. In this study, surface modification and hydrogen retention of a LHD divertor tile used for plasma experiments for 8 years were analyzed.

Fig. 1 shows surface morphology (a~d) and chemical composition (E, F) of the tile surface from the scanning electron microscope (SEM) and the energy dispersive X-ray spectroscopy (EDS), respectively. The left side of the photograph still keeps virgin graphite color, but the right side has changed to brown. These results indicate that the former is erosion dominant while the latter is deposition dominant area. In the deposition area, substantial amount of Fe and Ti were deposited. It seems that the Fe impurities came from the first wall during glow discharge cleaning (GDC) [2], and the Ti originated from Ti gettering operation which is often used to reduce oxygen impurities in the vacuum vessel. The surface at the erosion area (a), and (b), looks porous. This fact indicates strong sputtering erosion. The surface of the deposition area is covered by deposits with small hills of about 1-2μm in size. It seemed that mixed-material composed

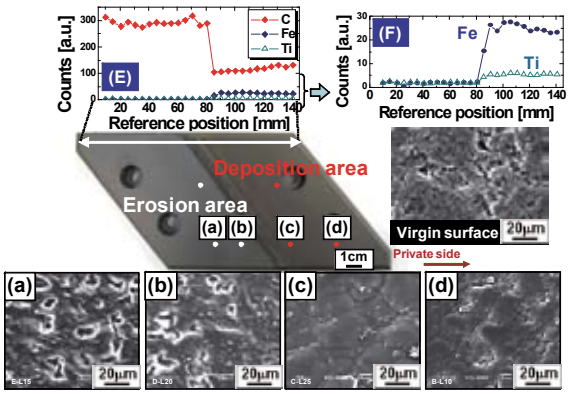

Fig. 1 SEM image of the surface (a~d) and distribution of the deposited elements (E, F).

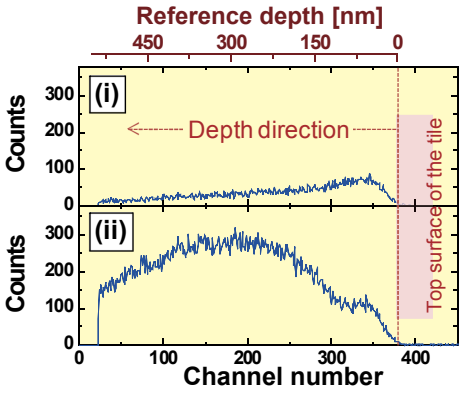

Fig. 2 ERD spectra of the retained hydrogen atoms from (i) erosion and (ii) deposition areas on the divertor tile.

of C, Fe and Ti of about a few μm thicknesses is formed on the surface of the (c) and (d).

Depth profile of hydrogen was measured by using an elastic recoil detection (ERD) technique. Fig. 2 shows ERD spectra from (i) erosion and (ii) deposition areas. A vertical axis (counts) and horizontal axis (channel number) corresponds to "the amount of hydrogen" and "the analyzed depth", respectively. Although in this figure, both axes were not converted to "the amount of hydrogen" and "the analyzed depth", because stopping power of the deposition layer could not be quantified yet. But if the stopping power of the fresh graphite crystal was assumed to conversion for the channel number (ch) to the depth (nm), the rate is roughly estimated to be 1.5nm/1ch. In order to make this figure more comprehensible, the reference depth estimated by using this rate was shown in the top of the figure. In the case of (i) erosion area, high counts of hydrogen concentration are observed at the depth of around ~50 nm and then, this is gradually decreased with increasing depth from the surface. However, the shape of the ERD spectrum of (ii) is much different from (i). A small peak was confirmed at the depth of around ~50 nm, and very high hydrogen concentration than (i) appeared with increasing the depth and kept up to the deep range. Judging from the connection length profile of the magnetic field lines crossing the divertor plate and probe measurements [3], influx of hydrogen on the deposition area is lower than that of the erosion area. Nevertheless retained hydrogen is much higher in the deposition side. This fact implies that the retention of hydrogen does not simply depend on its influx, but change of surface properties due to impurity deposition is important factor in determining hydrogen retention.

References

[1] M. Shoji et al., J. Nucl. Mater. 337-339 (2005) 186-190
[2] M. Tokitani et al., Nucl. Fusion 45 (2005) 1544-1549
[3] S. Masuzaki et al., Nucl. Fusion 42 (2002) 750-758

Key Words

Fusion Energy, Impurity Deposition, Hydrogen Retention

Contact to
Masayuki Tokitani (National Institute for Fusion Science)
e-mail: tokitani.masayuki@LHD.nifs.ac.jp
Shinji Nagata (Materials Design Division)
e-mail: nagata@imr.tohoku.ac.jp

Low Rigidity Titanium Alloy for Orthopedic Implant
Animal Study on Plate Fixation of Tibia Fracture Model in Rabbit

Because there is a big difference of material rigidity between living bone and conventional implant metals, orthopedic implant can induce bone atrophy due to decrease or absence of mechanical stress, so-called stress shielding. As a solution of the problem, a low rigidity titanium alloy of Ti-29Nb-13Ta-4.6Zr (TNTZ) was developed where the elastic modulus is 58 GPa and all elements are considered as non-toxic [1, 2].

In order to investigate bone tissue reaction to the low rigidity titanium alloy, animal study on plate fixation of rabbit tibia fracture model was performed [3]. Based on the design of commercial fixation device for human finger, Bone plate and screws were made of TNTZ (E=58 GPa), Ti-6Al-4V (E=108 GPa) and SUS316L (E=161 GPa) where the elastic modulus of human cortical bone is 10 ~ 20 GPa. As experimental animal, mature New Zealand white rabbits were used.

Under intra-venous anesthesia, the bone plate was provisionally placed and fixed by screws, then once removed. Upper one third of tibia was cut through by using oscillating saw where the cut position was corresponding to the center of the bone plate. However, fibula was kept intact. Finally, the bone plate was tightly fixed again by screws. (Fig.1)

Regarding fracture healing, there was no significant difference among SUS316L, Ti-6Al-4V and TNTZ. As a general time course, callus formation was observed at 2 weeks, which became distinct at 3 weeks. Bone union was obtained at 4 weeks, and the fracture line was hardly observed around 8 weeks. The trace of the experimental fracture was completely disappeared at 16 ~ 20 weeks. (Fig.2)

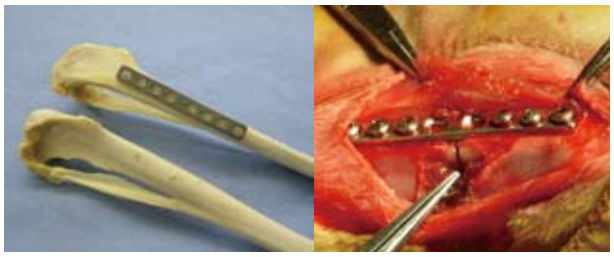

(a) Plate with dry bone . (b) Plate fixation.

Fig. 1 Plate fixation of rabbit tibia fracture model.

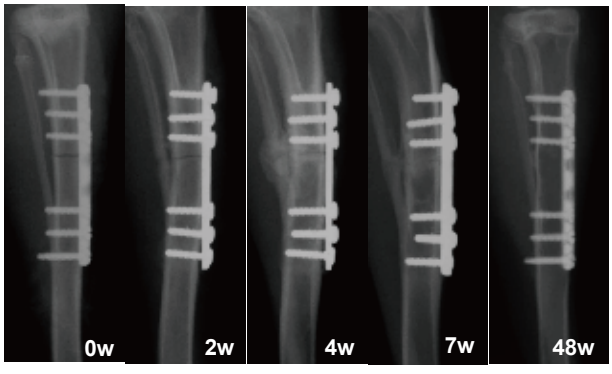

Fig. 2 X-ray follow-up for fracture healing and remodeling.

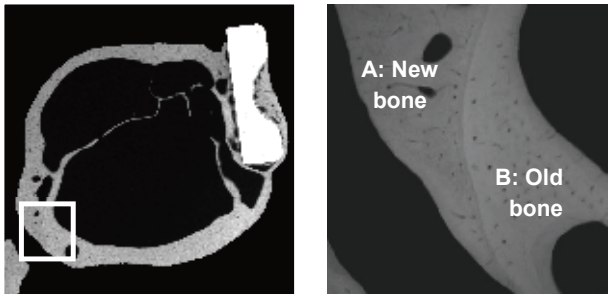

(a)Increase of tibia diameter (b) Close-up the junction

Fig. 3 Bone remodeling in TNTZ

However, bone atrophy was observed as porous or poor bone tissue in cortical bone especially under the bone plate, which was different in time course among three materials. In addition, the diameter of the tibia bone was increased by new bone formation in TNTZ, which seemed to be a result of bone remodeling. (Fig.3)

As the Wolff's law of the functional restoration, it is well known that the mechanical stress will influence the bone remodeling. According to this theory, the elastic modulus of the bone plate will naturally influence the bone tissue reaction in the bone plate fixation. However, since bone formation and remodeling is faster in small animals as compared with human and large animals, such remarkable bone atrophy was probably caused in a short periods of 48 weeks after the fixation.

From the results, it is suggested that low rigidity titanium alloy can delay or reduce bone atrophy in terms of retaining mechanical stress, and also promotes bone remodeling to adapt to new loading condition. Therefore the low rigidity titanium alloy of TNTZ is promising and applicable for implant metal, which provides a new option for fracture fixation.

References

[1] M. Niinomi, T. Hattori, S. Niwa, BIOMATERIALS IN ORTHOPEDICS:55-60, Marcel Dekker (2003)

[2] M. Niinomi, Materials Science and Engineering A, A243: 231-236 (1998)

[3] N. Sumitomo, K. Noritake, T. Hattori, K. Morikawa, S. Niwa, K. Sato, M. Niinomi, J Mater Sci: Mater Med 19:1581-1586 (2008)

Key words

Titanium Alloy, Low Rigidity, Orthopedic Implant

Contact to
Tomokazu Hattori (Department. of Materials Science and Engineering, Meijo University)
e-mail: tomhat@ccmfs.meijo-u.ac.jp
Mitsuo Niinomi (Biomaterials Science Division)
e-mail: niinomi@imr.tohoku.ac.jp

Large Tunnel Magnetoresistance in Magnetic Tunnel Junctions Using a Co_2MnSi Heusler Alloy Electrode and a MgO Barrier

A large tunnel magnetoresistance (TMR) ratio of 753% has been observed at 2 K in a magnetic tunnel junction (MTJ) using a Co_2MnSi Heusler alloy electrode and a crystalline MgO tunnel barrier. This TMR ratio is the largest reported to date in MTJs using a Heusler alloy electrode.

The development of ferromagnetic materials with high spin polarization is the most important subject in the spin electronics field. An ideal high spin polarization material is half-metallic ferromagnets (HMFs) with a band gap at the Fermi energy level for one spin band. Some full-Heusler alloys (Co_2MnSi, Co_2MnGe, etc.) are the most promising HMFs, because they have been predicted to possess a halfmetallic electronic structure and have a high Curie temperature. In addition, experimentally, we have observed large tunnel magnetoresistance (TMR) ratios of up to 159% at 2 K in magnetic tunnel junctions (MTJs) with Co_2MnSi/Al-O/CoFe structure; thus proving the halfmetallic property of Co_2MnSi (CMS). Although this TMR effect is pronounced in MTJs with a conventional amorphous Al-oxide barrier, recent work on MTJs with a MgO barrier showed better performance (Fig. 1). These results are suggested to be related to the coherent tunneling process through the MgO barrier. In addition, theoretically, Miura *et al.* showed that coherent tunneling through the MgO barrier could also occur and enhance TMR ratio in a CMS/MgO/CMS MTJ. In this work, we have succeeded in fabricating high-quality CMS/MgO/CoFe MTJs.

The MTJs with a structure of MgO (100) substrate/Cr (40) /Co_2MnSi (30) /MgO (2 - 2.5) /$Co_{50}Fe_{50}$ (5) /IrMn (10) /Ta (5) (unit: nm) were fabricated using an ultrahigh vacuum magnetron sputtering system [1]. The MgO tunnel barrier was formed by electron beam evaporation. The pressure during evaporation was about 2 x 10^{-6} Pa and typical evaporation rate was 0.01 nm/s. The MTJs were patterned into 8 x 8 – 90 x 90 μm^2 areas using photolithography and Ar ion etching. Patterned MTJs were annealed in the range of 300 - 485°C for 1 h in high vacuum by applying a 1 T magnetic field to improve the crystallinity of the MgO barrier. For comparison, CoFeB/MgO/CoFeB-MTJ was fabricated in the same conditions and both the TMR effect and the differential conductance were investigated.

A cross-sectional high-resolution transmission electron microscope (HRTEM) lattice image on a sample of T_a=450°C along the (110) direction of the CMS film is shown in the inset of Fig. 1. It confirmed that extremely smooth and abrupt interfaces were formed. Both good crystallinity and high (001) orientation of the MgO barrier can promote a coherent

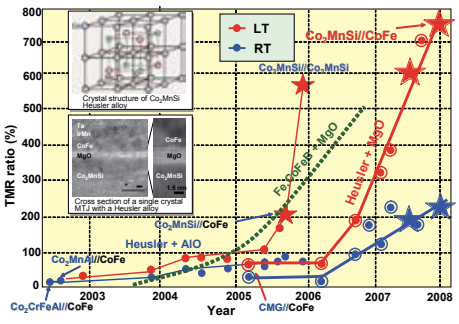

Fig. 1 Recent trend of TMR ratio of MTJs using a Co_2MnSi Heusler alloy electrode and an MgO (or Al-O) barrier.

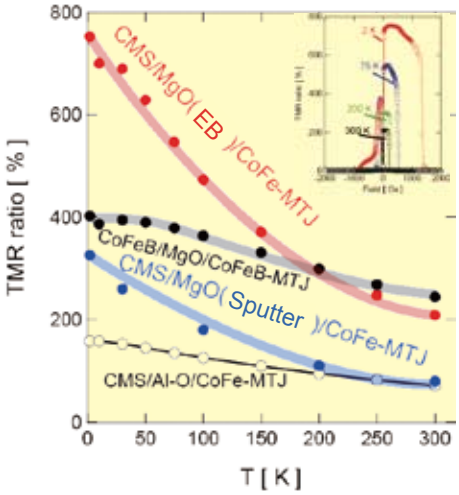

Fig. 2 Temperature dependence of TMR ritio for various MTJs.

tunneling process through the Δ1 band of CMS. We infer that the reduction in tunnel resistance by the coherent tunneling process enhances the TMR effect at RT, compared to the MTJs with an amorphous Al-oxide barrier.

Figure 2 shows the temperature dependence of the TMR ratio of the MTJ annealed at 475 °C. The MR curves measured at various temperatures are shown in the inset of Fig. 2. For reference, the temperature dependences for both CoFeB/MgO/CoFeB-MTJ and CMS/Al-oxide/CoFe-MTJ are shown together in Fig. 2. The TMR ratio of the CMS/MgO/CoFe-MTJ increased drastically with decreasing temperature, and a huge TMR ratio of 753% was observed at 2 K. The TMR ratio of 753% at 2 K is the highest in the MTJs using Heusler alloy electrodes and much larger than those of CoFeB/MgO/CoFeB-MTJ (400%) and CMS/Al-oxide/CoFe-MTJ (160%). This result reveals that the half metallicity of the CMS can be realized not only in the MTJ with an amorphous Al-oxide barrier but in the MTJ with a crystalline MgO barrier. The larger temperature dependence of the TMR ratio of the CMS/MgO/CoFe-MTJ [2, 3] than that of the CoFeB/MgO/CoFeB-MTJ should be solved for the application to devices.

References

[1] S. Tsunegi, Y. Sakuraba, M. Oogane, K. Takanashi, and Y. Ando, Appl. Phys. Lett. **93**, 112506 (2008).
[2] N. D. Telling, P. S. Keatley, G. van der Laan, R. J. Hicken, E. Arenholz, Y. Sakuraba, M. Oogane, Y. Ando, K. Takanashi, A. Sakuma, and T. Miyazaki, Phys. Rev. B **78**, 184438 (2008).
[3] N. D. Telling, P. S. Keatley, L. R. Shelford, E. Arenholz, G. van der Laan, R. J. Hicken, Y. Sakuraba, S. Tsunegi, M. Oogane, Y. Ando, K. Takanashi, T. Miyazaki, Appl. Phys. Lett. **92**, 192503 (2008).

Key Words

Heusler Alloy, Tunnel Magnetoresistance, Spintronics

Contact to
Yasuo Ando (Graduate School of Engineering, Tohoku University)
e-mail: ando@mlab.apph.tohoku.ac.jp
Koki Takanashi (Magnetic Materials Division)
e-mail: koki@imr.tohoku.ac.jp

Neutron Irradiation Effects in Graphite for Fusion Reactor Applications -Hydrogen Absorption, Diffusion and Annealing Effects-

Bulk hydrogen retention and absorption kinetics have been studied on graphite, which is one of the candidate materials for plasma facing walls in a fusion reactor. It is ascertained in this study that two kinds of hydrogen trapping sites exist and be additionally produced during neutron irradiation. The creation and annealing of these two trapping sites show quite different behavior.

Graphite and carbon fiber/carbon composites (CFCs) are principal materials for current fusion experimental devices due to high thermal conductivity and thermal shock resistivity. However, these materials degrade such various advantages by irradiation of neutrons originated from the fusion reaction of deuterium and tritium. Moreover, since carbon has a chemical affinity to hydrogen, it may cause high tritium inventory in plasma facing walls and a large amount of fuel gas recycling between fusion plasma and wall materials. The authors also have found out that neutron irradiation significantly raised hydrogen retention in graphite in previous studies. From the viewpoint of plasma density control and reducing the radioactive tritium inventory in plasma facing components, it is important to clarify the hydrogen behavior in these materials.

Fig.1 shows a model of hydrogen trapping and transport in graphite proposed by the authors. In an absorption process, hydrogen molecules penetrate easily through open pores and grain boundaries of graphite filler grains and reach the surface of the grain. Then, hydrogen will migrate into the filler grain apparently as molecule (in practice, sequence of dissociation and recombination) controlled by the diffusion process with an activation energy of 1.3 eV. The hydrogen will be trapped at outside edge surface of crystallites by a covalent bond with the adsorption enthalpy of 2.6 eV. This site has been named as trap 2. If the trap 2 sites are sufficiently fulfilled with hydrogen atoms, hydrogen can permeate into the crystallite along the graphite intercalations. The hydrogen absorption, or atmospheric hydrogen pressure decrease, in this stage is controlled by first-ordered chemical reaction, which caused by dissociation at a surface or detrapping from trap 2. Inside a crystallite, there are interstitial cluster loops or zigzag structures, and they should be the other trapping site for hydrogen (trap 1). The trap binding energy for hydrogen was estimated to be 4.4 eV. In the case of unirradiated samples, the number of trap 1 is below 10 % of the total number of trapping sites, and trap 2 is the major

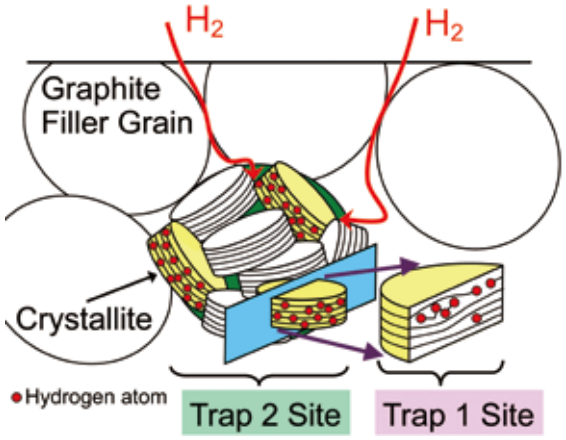

Fig. 1 Schematic illustration of hydrogen trapping sites and hydrogen transport in a graphite material.

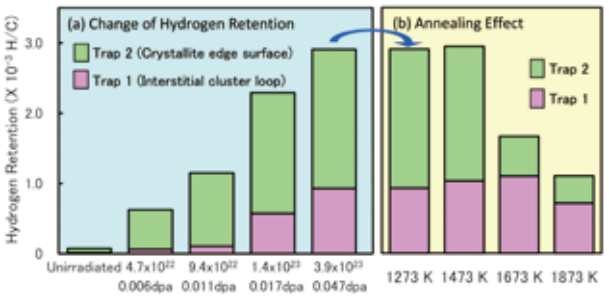

Fig. 2 Change of hydrogen retention and the pre-annealing effect in neutron-irradiated graphite shown for each trapping site (absorption temperature: 1273 K, Equilibrium pressure: ~ 10 kPa).

sites for hydrogen.

Graphite and CFC samples were irradiated in the Japan Materials Testing Reactor (JMTR) at various fluences up to 5.4 x 10^{24} n/m^2 (>1 MeV), which corresponded to 0.65 dpa, below 473 K. Hydrogen retention in neutron-irradiated graphite determined for each trapping site is shown for different neutron fluences in Fig. 2 (a). The total retention increases with the irradiation fluence. At lower neutron fluences below 0.011 dpa, the increase is mainly due to the increase of trapping in trap 2, while trap 1 retention is clearly increased at higher fluences above 0.017 dpa. At the highest fluence of 0.65 dpa, the total retention became 6.3 times as large as that for 0.047dpa, and the retention consisted of nearly the same quantity of trap 1 and trap 2 retention.

The retention obtained for the samples which were annealed before hydrogen absorption is shown in Fig. 2 (b). The retention which corresponds to trap 2 tends to decrease with the increase of pre-annealing temperature. This indicates that most of the trap 2 sites induced by neutron irradiation will be annealed out at high temperatures. However, the trap 2 sites may not be completely annealed out, since the retention was still larger than the amount obtained for the unirradiated samples, which was also pre-annealed at 1873 K. On the other hand, retention in trap 1 tends to remain relatively high even after the heat treatment at 1873 K. One can conclude the trap 1 sites should be thermally more stable than trap 2.

Although it is not mentioned in the article, hydrogen diffusion coefficients and reaction rate constants at trap 2 in neutron-irradiated graphite and their pre-annealing effects have been investigated. These results are described in refs [1] and [2].

References

[1] H. Atsumi, A. Muhaimin, T. Tanabe and T. Shikama, J. Nucl. Mater. **386-388**, 379 (2009).

[2] H. Atsumi, T. Tanabe and T. Shikama, J. Nucl. Mater. **390-391**, 581 (2009).

Key Words

Fusion Reactor Materials, Graphite, Irradiation Effects

Contact to

Hisao Atsumi (Department of Electric and Electrical Engineering, Faculty of Science and Engineering, Kinki University)

e-mail: atsumi@ele.kindai.ac.jp

Tatsuo Shikama (Nuclear Materials Science Division)

e-mail: shikama@imr.tohoku.ac.jp

^{27}Al NMR Study of Np-Based Superconductor $NpPd_5Al_2$

We have investigated a newly discovered Np-based heavy fermion superconductor $NpPd_5Al_2$ by means of ^{27}Al NMR. Our NMR data provide evidence for d-wave symmetry of the Cooper pairs. This result strongly suggests that 5f-electron spin fluctuations could play an important role in the superconductivity of $NpPd_5Al_2$ [1].

The actinide compounds with 5f electrons occupy a special position in research on condensed matter physics. The reason for this is that 5f electrons in actinides behave as though they are near the boundary between localized and itinerant character. The electronic properties of these actinides are often characterized by a so-called heavy fermion state at low temperatures. A recent discovery of considerable interest was that of superconductivity in the heavy fermion compound $PuCoGa_5$ in 2002, where the superconducting (SC) transition temperature T_c was found to be 18.5 K. Following that discovery, in 2007 the first Np-based, heavy fermion superconductor $NpPd_5Al_2$ was discovered with the relatively high T_c=4.9 K by D. Aoki et al [2]. $NpPd_5Al_2$ has a tetragonal crystal structure as shown in the inset to Fig. 2. The physical properties of the SC state in $NpPd_5Al_2$ are interesting, e.g. strong Pauli paramagnetic effect, first-order SC transition, and so on. Recently, we have investigated the superconductivity in $NpPd_5Al_2$ using the NMR technique.

Figure 1 shows a variety of symmetries for Cooper pairs in a superconductor. S-wave symmetry for the Cooper pairs is composed of an isotropic orbital form and a singlet spin state. On the other hand, p- and d-wave symmetries are characterized by anisotropic orbital forms with triplet (p) and singlet (d) spin states, respectively. In the figure, we also show the possible origin for the attractive force within a Cooper pair.

NMR is a powerful tool for investigating the symmetry of Cooper pairs. The orbital form of the Cooper pairs can be determined by measuring the temperature dependence of the nuclear spin-lattice relaxation rate $1/T_1$ below T_c. $1/T_1$ reflects the density of states near the Fermi level. On the other hand, the spin state of the Cooper pairs can be determined by measuring the Knight shift. The Knight shift is associated with a local field induced by the electron spins at a nuclear site.

Fig.2 shows the temperature dependence of $1/T_1$ through the SC transition. $1/T_1$ shows a sharp drop just below T_c without the coherence peak (dotted line in Fig. 2) characteristic of a conventional s-wave superconductor. The absence of

Symmetry of the Cooper pairs	*s* wave	*p* wave	*d* wave
Orbital form of the Cooper pairs		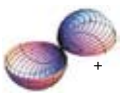	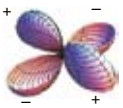
Spin state of the Cooper pairs	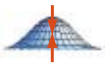 Spin singlet	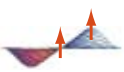 Spin triplet	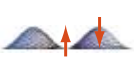 Spin singlet
Candidate for the origin of the attractive force	Phonon	Ferromagnetic fluctuations	Antiferromagnetic fluctuations

Fig. 1 Variety of symmetries for the Cooper pairs. The + and – show the sign of the wave function.

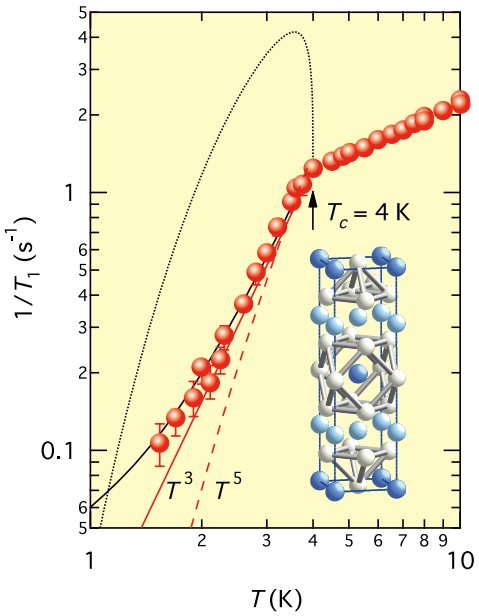

Fig. 2 Temperature dependence of $1/T_1$. Solid line shows calculation of $1/T_1$. Black dotted, red solid and red broken lines show calculated $1/T_1$ using full, line-node and point-node gaps, respectively. Inset shows the crystal structure of NpPd5Al2.

the coherence peak strongly indicates the occurrence of an anisotropic (non s-wave) SC state. The black solid line is a line calculated assuming a line-node in the SC gap. From the best fit to the experimental data, a relatively large value $2\Delta_0/k_BT_c$=6.4 of the SC gap has been obtained, which indicates strong coupling superconductivity. On the other hand, from the decrease of the Knight shift below T_c (not shown), we have confirmed a singlet spin state in $NpPd_5Al_2$. Therefore, our $1/T_1$ and Knight shift results strongly indicate d-wave superconductivity in $NpPd_5Al_2$. This suggests that the magnetic fluctuations of the 5f-electron spins plays an important role in the superconductivity of $NpPd_5Al_2$ [1]. We are currently investigating the characteristics of the magnetic fluctuations in the normal state.

References

[1] H. Chudo, H. Sakai, Y. Tokunaga, S. Kambe, D. Aoki, Y. Homma, Y. Shiokawa, Y. Haga, S. Ikeda, T. D. Matsuda, Y. Ōnuki, and H. Yasuoka, J. Phys Soc. Jpn. **77**, 083702 (2008).

[2] D. Aoki, Y. Haga, T. D. Matsuda, N. Tateiwa, S. Ikeda, Y. Homma, H. Sakai, Y. Shiokawa, E. Yamamoto, A. Nakamura, R. Settai, and Y. Ōnuki, J. Phys Soc. Jpn. **76**, 063701 (2007).

Key Words

Heavy-fermion, Superconductor, Transuranium Compound

Contact to
Hiroyuki Chudo (Advanced Science Research Center, Japan Atomic Energy Agency (JAEA))
e-mail: chudo.hiroyuki@jaea.go.jp
Yoshiya Homma (Radiochemistry of Metals Division)
e-mail: yhomma@imr.tohoku.ac.jp

A Novel Structure for Carbon Nanotube Reinforced Alumina Composites with Improved Mechanical Properties

We report the mechanical properties of multi-walled carbon nanotube (MWCNT) /alumina composites made with a pristine MWCNT and an acid-treated version that have nanoscale defects on their surfaces from an acid treatment. Mechanical measurements reveal that only 0.9 vol.% acid-treated MWCNT addition results in 27% and 25% simultaneous increases in bending strength and fracture toughness, respectively.

Carbon nanotubes (CNTs) have extremely high tensile strength and stiffness, good flexibility, and low density. These superior properties make CNTs attractive for many applications and technologies. Engineering ceramics have high stiffness, excellent thermostability, and relatively low density, but their brittleness impedes their use as structural materials. Incorporating CNTs into a ceramic matrix might be expected to produce tough as well as highly stiff and thermostable ceramic composites. Until now, however, most results for strengthening and toughening have been disappointing, and only little or no improvement of strengthening and toughening has been reported in CNT/ceramic materials. It is well known that the two problems exist in CNT/ceramic composite materials research. The first is the inhomogeneous dispersion of CNTs in the matrix. Pristine CNTs are well known for poor solubilization, which leads to phase segregation in the composite owing to the van der Waals attractive force. Severe structural inhomogeneities result in the degradation of the mechanical properties of the CNT composite materials [1]. The second problem is the poor connectivity between CNTs and the ceramic matrix, which leads to a limited stress transfer capability from the matrix to the CNTs. The connectivity with the matrix, and uniform distribution within the matrix are essential structural requirements for the stronger and tougher CNT/ceramic composites.

Here we report the mechanical properties of multi-walled carbon nanotube (MWCNT) /alumina composites made with a pristine MWCNT and an acid-treated version that have nanoscale defects on their surfaces from an acid treatment. A novel processing approach based on the precursor method can diminish the phase segregation of MWCNTs, and render MWCNT composites that are highly homogeneous [2]. Combined with a mechanical interlock induced by the chemically modified MWCNT, this approach leads to improved mechanical properties. Mechanical measurements on composites reveal that only 0.9 vol.% acid-treated MWCNT addition results in 27% and 25% simultaneous increases in bending strength and fracture toughness, respectively, indicating enhanced stress transfer capability from the alumina to the MWCNTs [2].

An interesting geometric structure was observed between

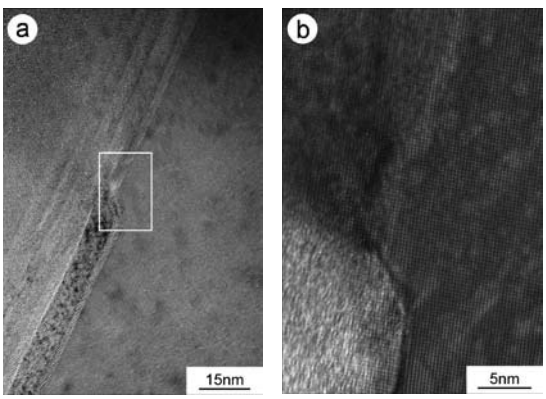

Fig. 1 MWCNT morphology in the composites. (a) It is demonstrated that a nanodefect on the acid-treated MWCNT is filled up with alumina crystal. (b) Enlarged TEM image, taken from the square area.

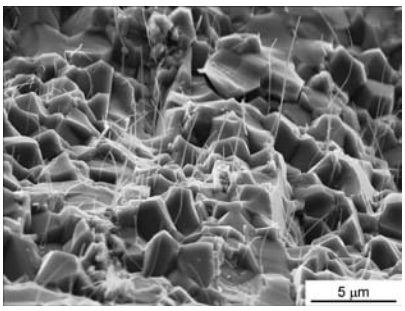

Fig. 2 Fracture surface of the acid-treated MWCNT/alumina composite. Numerous individual MWCNTs protrude from the fracture surface.

individual MWCNTs and alumina matrix, as shown in Figs. 1(a) and (b). It is revealed that a nanodefect on the acid-treated MWCNT is filled up with alumina crystal, which may be intruding into the nanodefect during grain growth. This nanostructure is novel in that its structure resembles a nanoscale anchor with an alumina crystal spiking the surface of the MWCNT. From the fracture surface, the following features can be noted. Numerous individual MWCNTs protrude from the fracture surface, and the pullout of the MWCNTs can be clearly observed, which had not been obtained until now for conventional CNT/ceramic composites (Fig. 2). Some MWCNTs showed that the diameter of pullout MWCNT drastically slenderized toward their tip[2], quite similar to that observed in a broken MWCNT under tensile load. This failure mode of the acid-treated MWCNT may be due to the enhancement of effective frictional resistance between individual MWCNTs and the alumina matrix. In the case of the smaller amount of the acid-treated MWCNTs, no phase segregation was observed, whereas the composites made with the pristine MWCNT revealed an inhomogeneous structure even for MWCNT addition as low as 0.9 vol.%. These observations revealed that the high structural homogeneity and enhanced frictional resistance of the structural components leads to a simultaneous increase in the strength and toughness of the acid-treated MWCNT/alumina composites.

Our present work may give a promising future for the application of MWCNTs in reinforcing structural ceramic components and other materials systems as well. The acid-treated MWCNT/alumina composites may have potential applications to tribomaterials such as joint prosthesis and micro electro mechanical systems (MEMS), because of the CNTs' good lubrication properties [3].

References

[1] G. Yamamoto, M. Omori, K. Yokomizo and T. Hashida, Diam. Relat. Mat. **17,** 1554 (2008).

[2] G. Yamamoto, M. Omori, T. Hashida and H. Kimura, Nanotechnology **19,** 315708 (2008).

[3] G. Yamamoto, T. Hashida, K. Adachi and T. Takagi, J. Nanosci. Nanotechnol. **8,** 2665 (2008).

Key Words:
Carbon Nanotubes, Alumina, Mechanical Properties

Contact to
Go Yamamoto (Institute of Fluid Science, Tohoku University)
e-mail: gyamamoto@rift.mech.tohoku.ac.jp
Hisamichi Kimura (Advanced Research Center of Metallic Glasses)
e-mail: hisami@imr.tohoku.ac.jp

Calcification by MC3T3-E1 Cells on RGD Peptide Immobilized on Titanium Through Electrodeposited PEG

The effect of a cell-adhesive peptide containing Arg-Gly-Asp (RGD) immobilized through poly (ethylene glycol) (PEG) on titanium (Ti) on calcification by MC3T3-E1 cells was investigated to develop a new surface modification technique using biofunctional molecules. The hard tissue compatibility of Ti is improved by immobilizing RGD through functional molecules which have a long molecular chain.

One terminal group of twitterions with a -COOH group and a -NH_2 group is useful to bond biofunctional molecules such as RGD. At a certain pH known as the isoelectric point (IEP), the -NH_2 group is positively charged and the -COOH group is negatively charged. On the other hand, the other terminal group is required to bind stably with a surface oxide on a metal. The surface oxide film of a metal is usually covered by hydroxyl groups. The hydroxyl groups are positively or negatively charged according to the pH of the surrounding solution. The surface charge is apparently zero at a certain pH that is known as the point of zero charge (pzc). Therefore, a zwitterion-mediated surface for the immobilization of biofunctional molecules such as RGD is created with consideration of the interaction between the charged zwitterion and the charged metal surface in a solution. A simple immobilization technique with consideration of the isoelectric point of molecules IEP and pzc is necessary.

The IEPs of two zwitterions, glycine and both-terminal-terminated PEG (NH_2-PEG-COOH) were determined from the titration curves, and the thickness of zwitterion layers immobilized on Ti with immersion and electrodeposition at various pH based on IEPs were evaluated with ellipsometry to investigate the effect of pH and the immobilization technique on the interactions between the zwitterions and Ti surface. From the titration curves, pK_1, pK_2, and the IEP of glycine were determined as 2.8, 8.9, and 5.9, respectively, and pK_1, pK_2, and the IEP of NH_2-PEG-COOH were determined as 2.1, 11.7, and 6.9, respectively (Fig.1). At a certain specific pH, ^+H_3N-CH2-COO^- or ^+H_3N-PEG-COO^- were formed by hydrolysis of glycine or NH_2-PEG-COOH. In addition, the Ti surface was negatively charged at this pH. As a result, for immersion, the electrostatic reactivity between terminal groups of zwitterion and hydroxyl groups on Ti surface was the highest and the thickness of the immobilized layer was significantly the largest

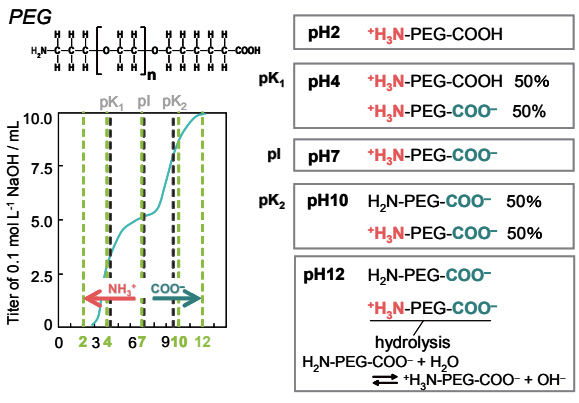

Fig. 1 Titration curve of PEG (NH_2-PEG-COOH) and effect of pH on dissociation of terminals of PEG.

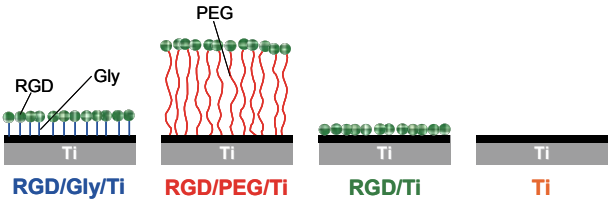

Fig. 2 Specimens employed in this study.

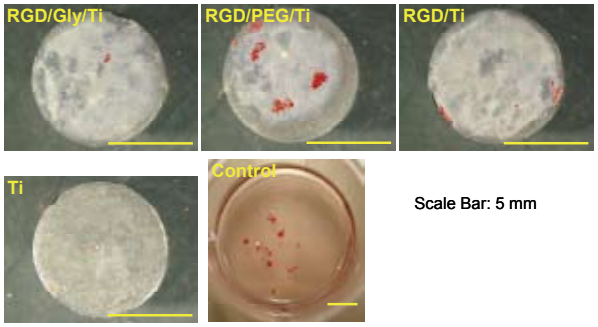

Fig. 3 Pictures of calcified deposits in MC3T3-E1 cells stained with a 1% alizarin red S solution after fixation. Calcified deposits are stained red.

at pH 12. For electrodeposition, glycine, with its smaller molecular weight, was more easily attracted to Ti surface than NH_2-PEG-COOH, which has a larger molecular weight, while the thickness of the immobilized layer was the largest at pH 12 in both zwitterions [1].

The effect of a cell-adhesive peptide containing RGD immobilized through PEG on Ti on calcification by MC3T3-E1 cells was investigated. RGD was immobilized on Ti through PEG. PEG was immobilized on Ti with electrodeposition, and RGD, with immersion. For comparison, glycine was employed because it is the simplest molecule containing both -NH_2 and -COOH at its terminals (Fig.2). MC3T3-E1 cells were cultured and differentiation-induced on each specimen, and the cell calcification properties were investigated. The level of cell calcification on RGD/PEG/Ti was the highest (Fig.3) [2].

References

[1] Y. Tanaka, H. Saito, Y. Tsutsumi, H. Doi, N. Nomura, H. Imai and T. Hanawa: J. Colloid Interface Sci. **330**, 138 (2009).

[2] K. Oya, Y. Tanaka, H. Saito, K. Kurashima, K. Nogi, H. Tsutsumi, Y. Tsutsumi, H. Doi, N. Nomura and T. Hanawa, Biomaterials **30**, 1281 (2009).

Key Words

Titanium, Biofunctional Molecule, Electrodeposition

Contact to
Takao Hanawa (Institute of Biomaterials and Bioengineering, Tokyo Medical and Dental University)
e-mail: hanawa.met@tmd.ac.jp
Hisamichi Kimura (Advanced Research Center of Metallic Glasses)
e-mail: hisami@imr.tohoku.ac.jp

Metallic Glass Components Produced by Rapid-Rotation Centrifugal Casting

"Rapid-Rotation Centrifugal Casting Process" was applied to manufacturing the amorphous bulk metallic glassy alloys (BMGs) components. The molten alloys were poured into copper mold with rotation speed over 3000rpm which can cause 100 times as much centrifugal pressurization force as gravity. The samples such as small gear, screw, biomedical artificial tooth-root model and gripper of endoscope of Zr or Fe alloy systems were successfully fabricated within only a few seconds at one process with more cheap cost.

Bulk metallic glassy alloys(BMGs) have the strong interest in material science and technology because they have the unique characteristics such as very high strength, high corrosion resistance, high wear resistance as well as the flexible workability based on viscous super-elasticity phenomenon of appearing near the glassy transition temperature T*g* of BMG. However, too much deformation process during this secondarily working for BMG will cause the nano-microscopic change of amorphous structure as well as the degradation of BMG's properties, therefore, new innovative material processing technique for mass-producing BMG components is becoming a important subject for commercial production of BMGs. Recently, an innovative "Rapid-Rotation Centrifugal Casting Process" to the components and commercial production of BMGs was developed [1]. The schematic figure of this method is schematically shown in Fig. 1.

The melted raw BMG alloys by high frequency induction heating method were poured into copper mold with changing the rotation speed over 3000rpm which can cause over 100 times as much centrifugal pressurization force as gravity.

The fabricated BMG component sample is shown in Fig. 2 where the produced artificial tooth model of Zr55Al10Ni5Cu30b are amorphous state as shown in XRD pattern.

The morphology is apt to change depending on the alloy composition and rotating speed of copper dies. Fig.3 shows the laser micrograph , XRD and picture of [(Fe0.5Co0.5)0.75 B0.2Si0.05]96Nb4 alloy.

In this case, outer part is almost amorphous and a partial crystallization is observed in inner part probably due to the difference of cooling capacity from copper mold. According to synergistic effect of rapid solidification and high pressurization casting in this manufacturing process, there are technical advantages of expansion of element composition, uniformity of the quality, reduction of internal defects and prevention of degradation at the time of secondary fabrication process of BMGs, which seems easy to automation, a large amount of cost cut and mass production in the very near future.

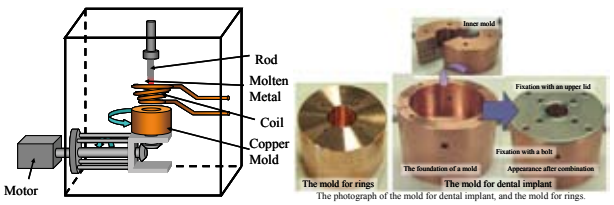

Fig. 1 Schematic view of the developed rapid-centrifugal casting for BMGs

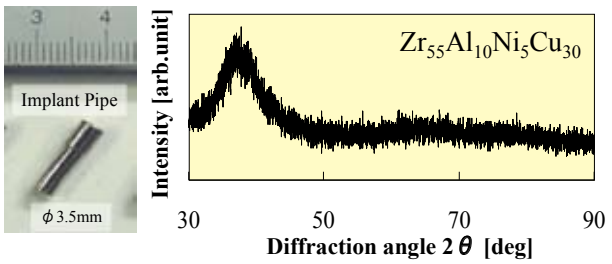

Fig. 2 Dental implant model and XRD of $Zr_{55}Al_{10}Ni_5Cu_{30}$

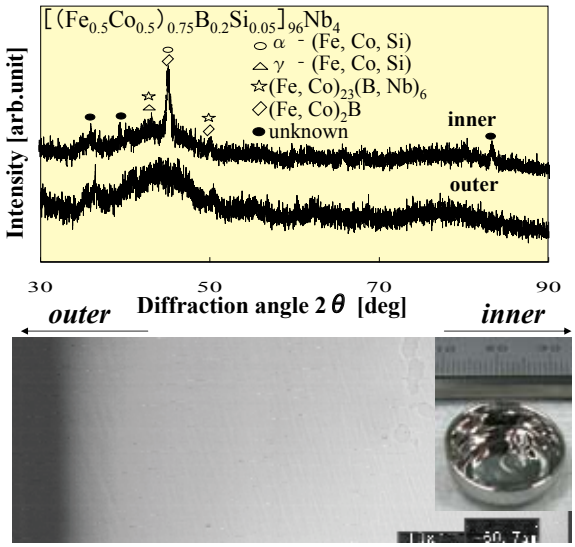

Fig. 3 Laser micrograph, XRD and picture of [(Fe0.5Co0.5) 0.75B0.2Si0.05] 96Nb4 alloy

References

[1] K. Hashimoto, T. Kubota, T. Mashiko, T. Okazaki, Y. Furuya and A. Inoue, J.Japan Inst. Metals. 71-7, 553-558 (2007)

Key words

Metallic Glass, Centrifugal Casting, Amorphous

Contact to
Yasubumi Furuya (Faculty of Science and Technology, Hirosaki University)
e-mail: furuya@cc.hirosaki-u.ac.jp
Hisamichi Kimura (Advanced Research Center of Metallic Glasses)
e-mail: hisami@imr.tohoku.ac.jp

In-Plane Electrical Resistivity in Magnetic Fields and Stripe Correlations in $La_{2-x}Sr_xCuO_4$ around $x = 0.21$

In recent years, magnetic-field effects on the so-called dynamical charge-spin stripe correlations, which might be in the heart of the mechanism of the high-T_c superconductivity, have been an issue of note. In contrast to the underdoped regime, the validity of the magnetic-field-induced stripes has been under debate in the overdoped regime due to lack of studies.

The application of magnetic field to the high-T_c superconductors leads to the creation of vortices in the superconducting (SC) state. In the vortices, scanning-tunneling-spectroscopy and neutron-scattering experiments have revealed the formation of a checkerboard-like charge order and a charge-spin stripe order as shown in Fig. 1, respectively. However, whether or not these are competing ordered states with superconductivity has not yet been clarified.

In order to investigate magnetic-field effects on the charge-spin stripe order from the viewpoint of transport properties, we previously measured the in-plane electrical resistivity, ρ_{ab}, in magnetic fields parallel to the c-axis for $La_{2-x}Ba_xCuO_4$ and $La_{2-x}Sr_xCuO_4$ (LSCO) around $x = 1/8$ [1,2]. It has been found for samples in which the charge stripe order is fairly stabilized that the SC transition curve sifts to the low-temperature side in parallel (parallel shift) with increasing magnetic field. These results suggest that the superconductivity with small SC fluctuations due to the short coherence length is realized in the stripe-ordered state.

As for the overdoped regime of LSCO around $x = 0.21$, significant anomalies have been observed so far; a slight depression of T_c [3], a development of the Cu-spin correlation at low temperatures [4] and an enhancement of the lattice instability by the application of magnetic field. These are suggestive of a possible development of the stripe correlations around $x = 0.21$ as well as around $x = 1/8$. Therefore, we have investigated magnetic-field effects on ρ_{ab} in LSCO around $x = 0.21$.

Single crystals used for the measurements were grown by the traveling-solvent floating-zone method. The ρ_{ab} measurements were performed in magnetic fields up to 27 T by the standard dc four-probe method, using a SC magnet below 17.5 T and a hybrid magnet above 17.5 T at the High Field Laboratory for Superconducting Materials (HFLSM), IMR, Tohoku University.

Figure 2 shows the temperature dependence of ρ_{ab} in LSCO with $x = 0.190$ - 0.215. With increasing magnetic field, the SC transition curve tends to show a parallel shift for $x = 0.206$ in which T_c is singularly depressed. For $x = 0.190$ and 0.215 in which no singular depression of T_c is observed, on the other hand, the SC transition curve shows rather

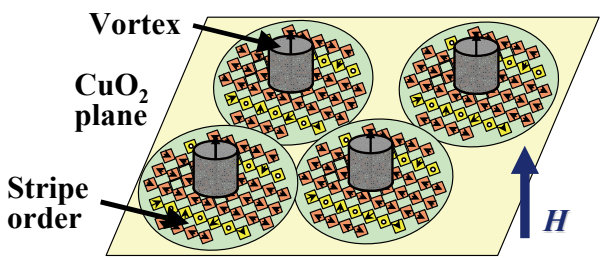

Fig. 1 Schematic picture of the formation of the stripe order around vortex cores in the CuO_2 plane of a high-T_c superconductor.

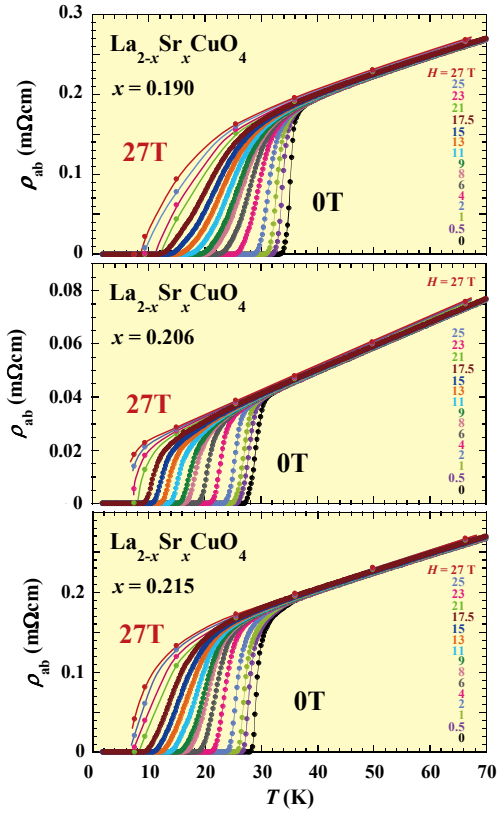

Fig. 2 Temperature dependence of the in-plane electrical resistivity, ρ_{ab}, in various magnetic fields along the c-axis up to 27 T for $La_{2-x}Sr_xCuO_4$ with $x = 0.190$ - 0.215.

broadening-like behavior. These results suggest that the superconductivity with small SC fluctuations is realized singularly around $x = 0.206$ in which T_c is depressed. Accordingly, it is concluded that the charge stripe order is singularly developed and is stabilized by the application of magnetic field in LSCO around $x = 0.21$.

References

[1] T. Adachi, N. Kitajima, T. Manabe, Y. Koike, K. Kudo, T. Sasaki, and N. Kobayashi, Phys. Rev. B **71**, 104516 (2005).
[2] T. Adachi, K. Omori, T. Kawamata, K. Kudo, T. Sasaki, N. Kobayashi, and Y. Koike, J. Phys.: Conf. Series **51**, 259 (2006).
[3] N. Kakinuma, Y. Ono, and Y. Koike, Phys. Rev. B **59**, 1491 (1999).
[4] I. Watanabe, M. Aoyama, M. Akoshima, T. Kawamata, T. Adachi, Y. Koike, S. Ohira, W. Higemoto, and K. Nagamine, Phys. Rev. B **62**, R11985 (2000).

Key Words

High-T_c Superconductivity, Stripe Order, Magnetic-Field Effect

Contact to
Tadashi Adachi (Department of Applied Physics, Tohoku University)
e-mail: adachi@teion.apph.tohoku.ac.jp
Norio Kobayashi (Low Temperature Physics Division)
e-mail: koban@imr.tohoku.ac.jp

Development of High-Field Scanning Tunneling Microscope for 18 T Cryocooled Superconducting Magnet

We have developed the high-field scanning tunneling microscope (STM) to study the nanoscale electronic order and the vortex state in high-T_c superconductors. Using the nonmagnetic vibration-isolation table, we have succeeded in observing STM atomic images in the magnetic field applied by the cryocooled superconducting magnet up to 18 T.

Scanning tunneling microscopy/spectroscopy (STM/STS) studies provide important information on the nanoscale spatial variation of the electronic state. In high-T_c superconductors (HTSC), the self-organized electronic patterns observed in the local density of states tend to appear when the superconductivity is suppressed, the magnetic field strong enough can be an important parameter to study the electronic state. To study the field dependence of nanoscale electronic states and the vortex state in HTSC in the high field region, we have developed a new STM system for the 18 T cryocooled superconducting magnet (18T-CSM) [1].

Figure 1 shows schematic illustration of the high-field STM system installed on the 18T-CSM at High Field Laboratory for Superconducting Materials, IMR, Tohoku University. The 18T-CSM is a large-scale magnet with a total weight of 5.8 tons, and the superconducting coils and a radiation shield are cooled by Gifford-McMahon-Joule-Thomson (GM-JT) cryocooler and two GM cryocoolers, respectively. It is expected that the mechanical vibration and/or sound generated from three cryocoolers become crucial noise for STM/STS measurements. To make a stable tunneling contact with atomic-scale stability, we have developed the compact vibration-isolation table which consists of the diaphragm type air springs. The vibration-isolation table should be completely nonmagnetic without any electric circuits because the stray field near the top flange becomes ~ 1 T when H = 18 T. As shown in the left photograph in Fig. 1, we have designed the small and rigid STM head (20mm in diameter × 55mm in length) to enhance the resonant frequency.

To evaluate the vibration noise of the 18T-CSM and the performance of the vibration-isolation table, we have measured the vibration acceleration signal by using a piezoelectric accelerometer and the FFT analyzer [1]. When the vibration-isolation table is not active, the STM atomic resolution is strongly hindered by the strong vibration noise from cryocoolers. However, the vibration noise is effectively reduced by the vibration-isolation table and the STM image shows atomic resolution. Figure 2 demonstrates the STM image of highly oriented pyrolytic graphite (HOPG) at H = 18 T. The STM image shows a clear atomic arrangement with a lattice constant of 2.5 Å for HOPG. The results indicate that the performance of STM does not degrade in high fields and the stray field (~ 0.2 T at the top part of the STM insert) does not affect very much on the preamplifier for the tunneling current signal. In this study, we have succeeded in expanding the field-range for STM measurements beyond the maximum field (H ~ 10 T) of previous STM studies.

We also performed continuous STM measurements in the field-sweep condition with a sweep rate of 18T/60min, in order to examine the stability of the STM operation in the magnetic field. In this condition, the deformation of the STM image is very small and the atomic arrangement is clearly resolved. These results indicate that the STM head developed in this study has a good stability in the scanning (x,y) and also feedback (z) directions even in the varying magnetic field. Since the STM system developed in this study is compatible with the 30 T hybrid magnet, we are planning to extend the possible field-range for STM/STS up to 30 T in the future.

References

[1] T. Nishizaki and N. Kobayashi, Journal of Physics: Conference Series **150**, 012031 (2009).

Key Words

Scanning Tunneling Microscopy, High Field, Cryocooled Superconducting Magnet

Contact to
Terukazu Nishizaki (Low Temperature Physics Division)
e-mail: terukazu@imr.tohoku.ac.jp

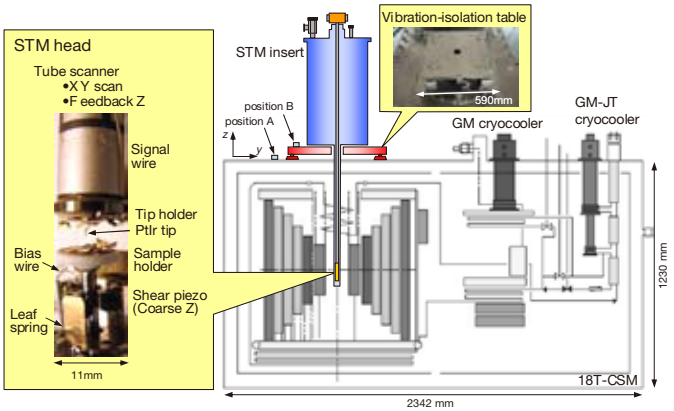

Fig. 1 Schematic illustration of the high-field STM installed on the 18T-CSM. Main parts for the STM head are shown in the left photograph. The nonmagnetic vibration-isolation table (upper right photograph) is set up between the 18T-CSM and the STM insert.

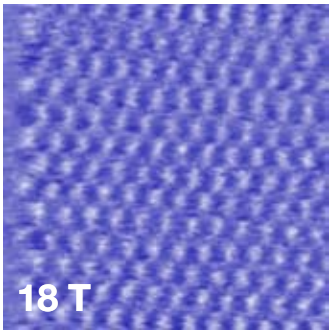

Fig. 2 STM image of HOPG (I = 0.1nA, V = 200mV) at H = 18 T. 35.4 Å × 35.4 Å.

Development of Hydroxyapatite Modified with Additives for High Performance Bioceramics

The hydroxyapatites modified with Si were synthesized by the normal heat-treatment in air atmosphere. The microstructures of these modified hydroxyapatites were characterized. XAFS study for these modified hydroxyapatites indicated the effect of Si on Ca-local structure of hydroxyapatite.

Hydroxyapatite (HAP) is a major inorganic component of bone and teeth, as shown in Figure 1. It possesses high biocompatibility as a biomaterial for implant part, bone filler, and bone-cement, etc. However, the achievement of the higher bioactivity for HAP is still demanded as a high performance bioceramic. In our group, the syntheses of HAP substituted with other metals have been attempted by various synthetic process, such as hydrothermal treatment, ion-exchange treatment, and normal heat-treatment at high temperature to enhance the bioactivity of HAP [1, 2, 3]. Thus, the syntheses of modified HAPs have been attempted by various processes, since the substitution with other metals in HAP is expected to improve the ability of bioactivity of HAP. In this study, the Si incorporated HAP were successfully synthesized by the normal heat-treatment and the effect of Si addition on micro- and local structure of HAP was clarified.

Commercial monolithic HAP powder was used as a starting material. Commercial SiO_2 powder (3, 10, and 30wt%) was added into HAP powder and mixed in ethanol with ball milling for 24h. Mixed HAP/SiO_2 powder was compacted with stainless mold and heat-treated at various temperatures in air atmosphere. The component of samples was identified with XRD. The microstructure of samples was observed by SEM and TEM. The local structure of Ca-*K* edge for samples heat-treated at 600 to 1200°C in air atmosphere was examined with XAFS (X-ray absorption fine structure) measurement at SPring8 in Kouto (Hyogo, Japan) and also at Photon Factory in Tsukuba (Ibaragi, Japan).

From XRD results of HAP samples containing with 3 to 30wt% SiO_2, monolithic HAP samples heat-treated at 600 to 1200°C were composed of hydroxyapatite phase without another calcium phosphate phase. HAP/SiO_2 samples heat-treated at 1200°C were composed of mainly α-tricalcium phosphate and in part hydroxyapatite, although the component of samples was composed of monolithic hydroxyapatite heat-treated below 1200°C. Thus, it was found that SiO_2 addition into HAP enhanced the formation of α-tricalcium phosphate above1200°C. According to FT-IR spectra of HAP/SiO_2 samples heat-treated at 1000°C with various SiO_2 content, HAP/SiO_2 samples with higher SiO_2 content indicated the stronger peak from SiO_4^{4-} with SiO_2 content. However, the peak form phosphate (PO_4^{3-}) for HAP/SiO_2 samples decreased with increase of SiO_2 content. In addition, the peak from OH^- for HAP/

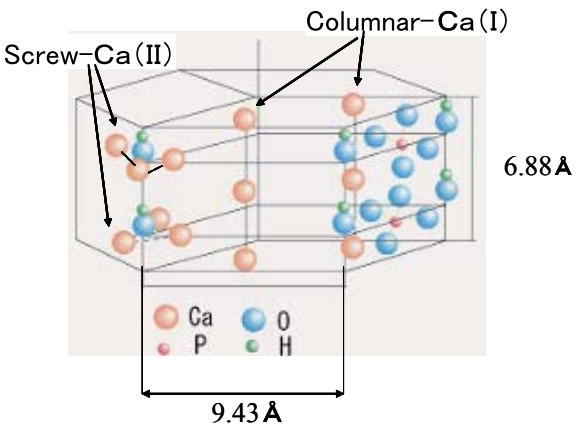

Fig. 1 Schematic drawing of hydroxyapatite (HAP) structure

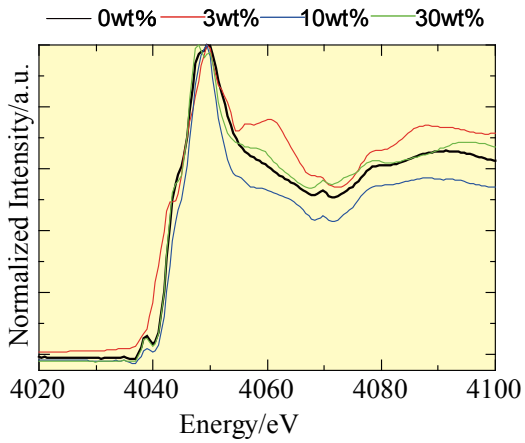

Fig. 2 XANES of Ca-edge for HAP samples with 3 to 30 wt%-SiO_2 heat-treated at 1200°C

SiO_2 samples decreased with high SiO_2 content of 30%. Since XRD results indicated no formation of calcium silicate in this study, it is speculated that this decrease in the peak from OH^- resulted from the formation of calcium silicate caused by the reaction HAP and SiO_2 content. Therefore, FT-IR results indicate that SiO_4^{4-}, below the optimum SiO_2 contents, was substituted for PO_4^{3-} site in hydroxyapatite structure during the heat-treatment at 1000°C.

Figure 2 shows the spectra of XANES of Ca-*K* edge for HAP samples with 3 to 30 wt%-SiO_2 heat-treated at 1200°C. HAP/3wt%SiO_2 samples heat-treated at 1200°C indicate the different spectra from monolithic HAP and HAP/10~30wt%SiO_2 samples. This result indicated that local structure around Ca-*K* edge was significantly different from monolithic HAP and also those from HAP containing with large amount of SiO_2 (10 to 30wt%) heat-treated at 1200°C. These XANES results also suggest that SiO_4^{4-} was substituted for PO_4^{3-} in hydroxyapatite structure. Thus, XANES results are consistent with the results of FT-IR. In special, the results of derivative from the normalized spectra for HAP/3wt%SiO_2 samples were clearly varied form others. The detailed examinations of Si-*K* and P-*K* are still attempted at another synchrotron facility. Thus, both XANES and FT-IR results indicated the noticeable structural changes accompany the substitution of SiO_4^{4-} into PO_4^{3-} site in hydroxyapatite structure. In addition, the bioactivity for these HAP modified with Si was excellent. As a result, it was found that these HAP modified with Si possess higher bioactivity, compared to monolithic HAP.

References

[1] A. Nakahira, S. Nakamura, and M. Horimoto, IEEE Transactions on Magnetics, 43[6], 2465-67 (2007).
[2] A. Nakahira, M. Horimoto, S. Nakamura, S. Ihshihara, H. Nagata, T. Kubo, and C. Karatani, *J. Ion Exchange*,18, 306-309 (2007).
[3] A. Nakahira, T. Okajima, T. Honma, S. Yoshioka, and I. Tanaka, Chemistry Letters, 35, 856-857 (2006).

Key Words

Bioceramics, Hydroxyapatite, Microstructure

Contact to
Atsushi Nakahira (Graduate School of Engineering, Osaka Prefecture University)
e-mail: nakahira@mtr.osakafu-u.ac.jp
Takashi Goto (Multi-Functional Materials Science Division)
e-mail: goto@imr.tohoku.ac.jp

New Metallic Carbon K4 Crystal

It has been successfully shown theoretically that the third structure of carbon crystals, K4, after diamond and graphite should exist by the CREST team in Tohoku University headed by Prof. Kotani with IMR members using our supercomputer SR11000 at the Center for Computational Materials Sciences. This K4 carbon crystal has an atomic structure in 3 dimensional space composed with sp^2 bondings between all carbon atoms, different from 2 dimensional structure of graphite. Diamond has also completely different which composed of sp^3 bondings. This K4 crystal is metallic in nature, and it is expected that by doping we can create stable superconductor, macroscopic conducting line, etc. which have been difficult to be realized by pure carbon nanostructures.

Recently, Prof. Sunada indicated by mathematical analysis[1] the sp^2 bonded systems with an attractive 3D structure, K4 crystal, which corresponds to the third crystal structure after diamond and graphite of carbon. An *ab initio* computer simulation has been conducted to apply this finding to a real material; carbon crystal. [2]

Figure 1 shows the K4 crystal structure, which is composed of 10 membered rings of carbons with all sp^2 bondings.

A possibility of pressure-induced structural phase transition between different crystal structures was investigated to confirm whether the K4 crystal is produced or not, by using a thermodynamic phase transition theory. According to this theory, negative slope of the tangent line between the energy vs volume curves of two different crystals indicates the positive transition pressure P_t which allows pressure induced structural phase transition between them. To the K4 crystal, it is apparent that P_t takes positive value only from graphite crystal with pressure induction parallel to the *a* axis as shown in Fig. 2.

According to the phonon calculation for the pure K4 carbon crystal, this crystal structure is indicated to have imaginary frequencies and should be unstable. We are now trying to expand the unit cell and find out not exactly K4 but more complex crystal structure around K4 which is more stable than K4 carbon crystal. Since K4 carbon crystal is metallic, there are many possibilities of K4 crystal for applications. Especially doping of atoms makes it possible to stabilize the system and to add more functionality such as superconductivity.

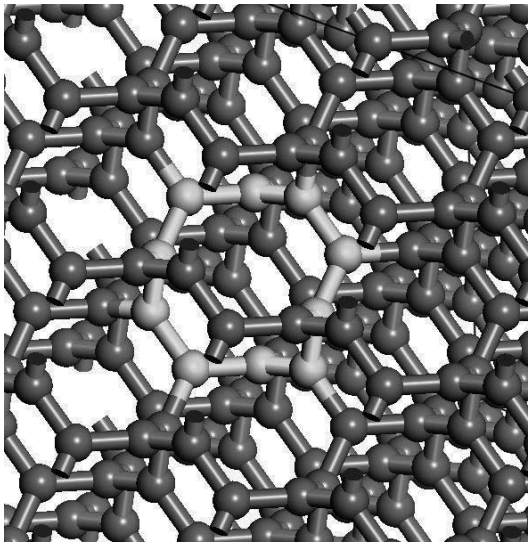

Fig. 1 K4 carbon crystal structure, which is composed of 10 member rings with all sp^2 bondings.

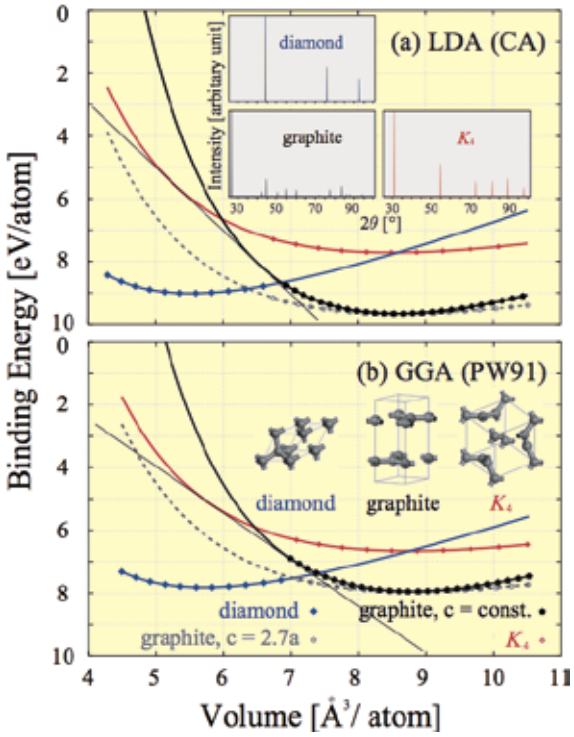

Fig. 2 Binding energy vs. volume curves of diamond (blue), graphite (grey, and black), and K4 (red) crystal structures composed of carbon atoms based on (a) LDA, and (b) GGA developed by Ceparley and Alder (CA), and Perdew and Wang (PW91) ; The curves are fits of the Murnaghan's equation of state to the calculated points. Tangential line between the curves of K4-graphite crystals; XRD patterns (in the inset of (a)).

References

[1] T. Sunada, Not. Amer. Math. Soc., 55, 208 (2008).

[2] Masahiro Itoh, Motoko Kotani, Hisashi Naito, Toshikazu Sunada, Yoshiyuki Kawazoe and Tadafumi Adschiri, Phys. Rev. Lett., **102**[5] (2009) pp.0557031-0557034

Key Words

Carbon Nanostructure, K4 Symmetry, Metallic Carbon

Contact to

Yoshiyuki Kawazoe (Materials Design by Computer Simulation Division)

e-mail: kawazoe@imr.edu

Optical Conductivity in the *t-J* Holstein Model

Using recently developed numerical method we compute optical conductivity of the t-J model coupled to optical phonons. Near the crossover to the strong electron-phonon coupling regime, optical conductivity shows a two-peak structure. This finding suggests that in the framework of the t-J Holstein model the two peak structure seen in recent optical measurements is due to magnetic excitations coupled to lattice degrees of freedom via doped charge carriers [1].

The enhanced interest in correlated models, coupled to lattice degrees of freedom is primarily fuelled by experimental evidence given in part by angular resolved photoemission data demonstrating that strong electron-phonon (EP) interaction plays an important role in low-energy physics of high-T_c materials. Using a numerical method based on the exact diagonalization within the limited functional space (EDLFS) [2, 3] we investigate optical properties of the *t-J* Holstein model for the case of a single hole in the antiferromagnetic background.

Figure 1 shows the influence of increasing EP coupling λ on optical properties of the *t-J* Holstein model in the adiabatic regime. Increasing λ leads to three main effects: a) the spectra progressively shift towards higher frequencies while the total spectral weight decreases; b) magnetic excitations that form a band in the mid-infrared (MIR) regime broaden and diminish with increasing λ; c) a large gap opens in the SC regime.

We find quantitative agreement at λ~0.24 with measurements on $(Eu_{1-x}Ca_x)Ba_2Cu_3O_6$ in the low hole-doping regime. In our calculation λ~0.24 represents the maximum EP coupling constant where the low-ω peak, located at ω_I, is just barely visible. This peak is due to the local magnetic excitation and remains separated from the continuum forming the rest of the MIR band. The higher-ω peak at ω_{II} corresponds to MIR band, broadened and renormalized by phonon excitations. Our explanation of the experimental results relies on the

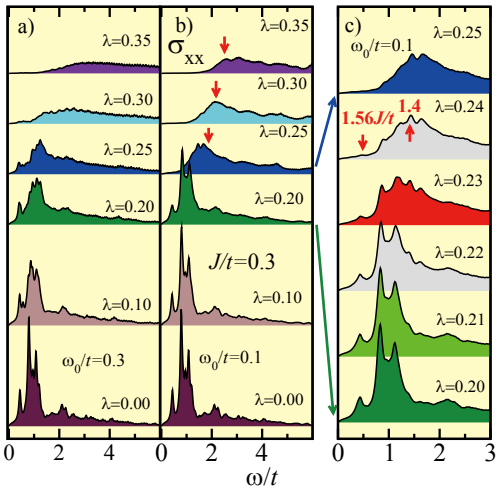

Fig. 1 Optical conductivity σ_{xx} for ω_0/t=0.3 in (a), ω_0/t=0.1 in (b) and (c) at J/t=0.3 and at **k**=(π/2,π/2). Up to 56 phonon quanta were used to obtain accurate results for λ>0.2. Arrows in (c) indicate ω_I~1.56J~187 meV (choosing t=400 meV and J/t=0.3) and ω_{II} ~1.4t~560 meV.

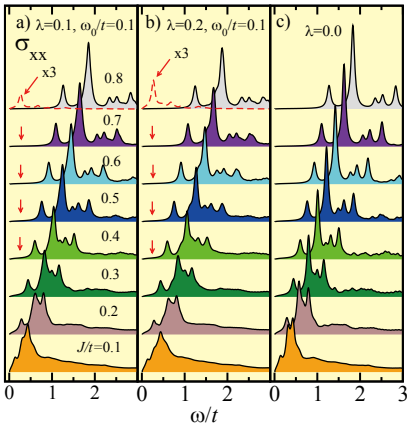

Fig. 2 σ_{xx} for ω_0/t=0.1 and λ=0.1 in (a), λ=0.2 in (b) and λ=0.0 (c) at **k**=(π/2,π/2) and different values of the exchange interaction J/t. Dashed lines, multiplied by a factor of 3 for better visibility, in (a) and (b) represent results of the Holstein model with ω_0/t =0.1 calculated at corresponding values of λ and **k**=(0,0). Arrows in (a) and (b) indicate the position of the lowest-ω peak for the Holstein model.

conjecture that lightly doped $(Eu_{1-x}Ca_x)Ba_2Cu_3O_6$ compound lies in the crossover from weak to strong coupling electron-phonon regime where physical properties (quasiparticle weight, charge stiffness and dynamic properties) are extremely sensitive to small changes of λ.

The lack of low-frequency peak above $\omega=\omega_0$ associated with phonon excitations in the limit of weak EP coupling is investigated in Figure 2. We have applied EDLFS method to solve the Holstein model with a single electron using essentially identical Hilbert space describing lattice degrees of freedom as the one used for the *t-J* Holstein model. $\sigma_{xx}(\omega)$ is for this case presented with dashed lines. We present optical spectra for various values of magnetic exchange interactions J/t of the *t-J* Holstein model. By increasing J/t magnetic peaks shift towards higher frequencies that should separate magnetic and lattice degrees of freedom. Nevertheless, we observe no signature of peaks above $\omega=\omega_0$ as they would appear in the corresponding Holstein model.

Authors acknowledge the hospitality of IMR, Tohoku University, where this work has been initiated.

References

[1] L. Vidmar, J. Bonča and S. Maekawa, Phys. Rev. B **79**, 125120 (2009).

[2] J. Bonča, S. Maekawa and T. Tohyama, Phys. Rev. B **76**, 035121 (2007).

[3] J. Bonča, S. Maekawa, T. Tohyama and P. Prelovšek, Phys. Rev. B **77**, 054519 (2008).

Key Words

Optical Conductivity, *t-J* Holstein Model, Strong Correlations

Contact to
Sadamichi Maekawa (Materials Property Division)
e-mail: maekawa@imr.tohoku.ac.jp